scientific reports

OPEN

Metal chalcogenides (CuS or MoS$_2$)-modified TiO$_2$ as highly efficient bifunctional photocatalyst nanocomposites for green H$_2$ generation and dye degradation

Reem A. El-Gendy[1,2✉], Haitham M. El-Bery[1,2✉], Mostafa Farrag[3] & Dina M. Fouad[3]

Herein, we report the modification of TiO$_2$ nanostructures with two different metal chalcogenides (CuS or MoS$_2$). The effect of the preparation scheme (hydrothermal and coprecipitation methods) and the mass ratio of metal chalcogenides were investigated. The as-synthesized photocatalyst nanocomposites were fully characterized by various techniques. Moreover, the photo/electrochemical analysis were performed to investigate the photoelectric properties and photocatalytic mechanism. The photocatalytic performance was evaluated using two test reactions. In the case of H$_2$ generation via water splitting, it was found that 0.5 wt% CuS-TiO$_2$ synthesized via the coprecipitation method exhibited an initial hydrogen evolution rate (HER) of 2.95 mmol h^{-1} g^{-1}. While, the optimized 3 wt% MoS$_2$-TiO$_2$ synthesized by the hydrothermal method, showed an HER of 1.7 mmol h^{-1} g^{-1}. Moreover, the degradation efficiency of methylene blue dye was 98% under UV–Vis light irradiation within 2 h over 0.5 CT_PP and 3MT_HT. Under visible irradiation, the degradation efficiency was 100% and 96% for 3MT_PP and 0.5CT_HT in the presence of H$_2$O$_2$, respectively. This study has proven that metal chalcogenides can act as effective, stable, and low-cost bifunctional co-catalysts to enhance the overall photocatalytic performance.

The accessibility of clean water and renewable energy sources are considered two of the major challenges facing humanity in the twenty-first century[1]. Nowadays, the development of industry depends strongly on fossil fuels. However, the fossil fuel sources may be depleted in the future. Moreover, the increasing utilization causes extensive greenhouse gas emissions. The development of eco-friendly and environmentally source of energy is highly desirable. Recently, Semiconductor-based photocatalysis has been investigated a promising strategy for water purification and hydrogen production[2,3].

Since the pioneering work by Honda and Fujishima in 1972 in the splitting of water over n-type TiO$_2$ electrodes[4], several studies have been carried out to explore suitable materials. Many semiconductors, TiO$_2$, CdS, and ZnO, have been developed for hydrogen generation and water treatment[5].

TiO$_2$ is considered as the most extensively used photocatalyst because of its availability, great chemical stability, and non-toxicity[6–8]. However, TiO$_2$ suffers from an insufficient response to visible light because it has a wide band gap ($E_0 = 3.2$ eV), the high recombination rate of photoexcited charge carriers, and the rapid reverse reaction. Thus, several attempts have been made to enhance the photocatalytic activity of TiO$_2$[9–12]. Due to these limitations, several schemes have been made to alter TiO$_2$ with noble metals (e.g., Pt, Pd, Au, and Ag)[13,14], transition metals (e.g., Cu and Ni)[15,16] and their oxides (e.g., NiO and CoO$_x$)[17,18], dye sensitization[19] and the construction of heterojunctions with other semiconductors[20,21]. Many studies employed noble metals and their oxides (e.g., Pt, Pd, RuO$_2$, and Ag$_2$O)[14,22–24] as potential co-catalysts to elevate the photocatalytic activity of TiO$_2$. However, noble metals are very expensive; thus, modification with non-noble metals as a co-catalyst is urgent.

In recent years, metal chalcogenides photocatalysts, such as CdS, CuS, MoS$_2$, and ZnS, have attracted a considerable attention due to their efficient photocatalytic activity toward water splitting and wastewater treatment.

[1]Advanced Multifunctional Materials Laboratory, Chemistry Department, Faculty of Science, Assiut University, Assiut 71515, Egypt. [2]Basics Science Department, School of Biotechnology, Badr University in Assiut, Assiut 2014101, Egypt. [3]Department of Chemistry, Faculty of Science, Assiut University, Assiut 71516, Egypt. ✉email: reem.abdellah@bua.edu.eg; Haitham.El-Bery@aun.edu.eg

These properties can be explained owing to their narrow band gaps, suitable physical and chemical structure, sufficient thermal stability and good response to visible light[25–28]. Therefore, the coupling of metal sulfides with TiO$_2$ has played a crucial role encouraging the separation of photogenerated electron–hole pairs and elevating the photocatalytic activity for dye degradation and hydrogen generation. Among these metal sulfides, CuS is a metal sulfide semiconductor with a narrow band gap (2.0–2.2 eV), which is nontoxic, cheap and available[29]. Moreover, CuS/TiO$_2$ form type II heterojunction as a result the separation of the photoexcited carriers has been improved. For MoS$_2$, it is a 2D layered structure semiconductor with an indirect band gap of 1.2 eV and a direct band gap in the mono-layered form of 1.8 eV. Hu et al. reported that MoS$_2$ nanosheets dramatically enhance the performance of CdS to 49.8 mmol h^{-1} g^{-1} for photocatalytic H$_2$ evolution[30]. Furthermore, MoS$_2$ has also been investigated to be coupled with TiO$_2$ to enhance the photocatalytic hydrogen generation and dye degradation under the irradiation of both ultraviolet and visible light[31,32]. Although, many reports have studied the improved photocatalytic activity of TiO$_2$ modified with metal sulfides, these studies focused mainly on synthesis methods involving long preparation times and high-temperature conditions. The facile coprecipitation method is a simple technique to prepare TiO$_2$ loaded by CuS and MoS$_2$ co-catalysts with high activity toward H$_2$ generation and dye degradation.

Herein, we demonstrate the modification of TiO$_2$ using metal sulfides (MS$_x$) co-catalysts (MoS$_2$ and CuS) via two different preparation methods: hydrothermal method (HT) and coprecipitation method (PP) with varying the weight ratios of MS to TiO$_2$. The H$_2$ generation via water splitting was performed under the irradiation of UV light and methanol as a scavenger reagent. Meanwhile the photocatalytic degradation of methylene blue (MB) aqueous solution was performed under both UV–Vis and only Vis irradiation. Also the Photoelectrochemical measurements PEC have been studied. The characterization and the probable reaction mechanism of the as-prepared photocatalysts are discussed in detail.

Experimental section

Materials. TiO$_2$ Aeroxide p25 (ACROS ORGANICS), Cu(NO$_3$)$_2$·3H$_2$O (> 95%), (NH$_4$)$_6$Mo$_7$O$_{24}$·4H$_2$O (<95%) were obtained from Fisher chemicals, Na$_2$S (99%, ALPHA CHEMICALS), C$_2$H$_5$NS (98%, Alfa Aesar), H$_2$O$_2$, methanol, and MB was obtained from Sigma–Aldrich. All the reagents were of analytical grade and used as received without further purification.

For comparison purposes metal chalcogenides MS$_x$ (CuS or MoS$_2$) were loaded over TiO$_2$ via two different methods, namely, hydrothermal treatment and coprecipitation methods. The detailed synthesis procedure is illustrated as follows.

Preparation of MS$_x$ (CuS or MoS$_2$)/TiO$_2$ by hydrothermal method. The MS$_x$/TiO$_2$ photocatalysts were synthesized through a simple hydrothermal treatment procedure[33]. Typically, TiO$_2$ p25 powder was dispersed in 70 mL deionized (DI) water and ultrasonically treated for 10 min, then various quantity ratios of Cu(NO$_3$)$_2$·3H$_2$O or (NH$_4$)$_6$Mo$_7$O$_{24}$·4H$_2$O and an excess of C$_2$H$_5$NS (Cu/S, Mo/S = 1:2, 1:5 molar ratio, respectively) were dropped slowly onto the above solution. The mixed solution was stirred for 1 h. Subsequently, the mixture was poured into a Teflon-lined autoclave and heated at 160 °C for 12 h (CuS/TiO$_2$) and 180 °C for 24 h (MoS$_2$/TiO$_2$). The resulting product was separated by centrifugation, washed several times with ethanol and water, and dried overnight at 80 °C in air. The resulting photocatalysts were labeled xCT_Z, and yMT_Z, where x = (0.3%, 0.5%, 0.7% and 1.0%); y = (1.0–4.0%) are the weight percent of the hetero-photocatalyst and CT represents CuS/TiO$_2$, MT means MoS$_2$/TiO$_2$, while Z is the preparation method: HT for hydrothermal treatment method and PP for the coprecipitation method.

Preparation of MS$_x$ (CuS, MoS$_2$)/TiO$_2$ by coprecipitation method. In a typical procedure, TiO$_2$ p25 was dispersed in 100 mL (DI) water and sonicated for 10 min, and then Cu(NO$_3$)$_2$·3H$_2$O or (NH$_4$)$_6$Mo$_7$O$_{24}$·4H$_2$O were added and stirred for 30 min after that, a Na$_2$S solution was added to the overhead mixture and stirred vigorously for 1 h. The precipitate was washed by centrifugation with ethanol and distilled water, finally dried at 80 °C overnight. In the case of MoS$_2$/TiO$_2$ 1 ml of HCl (1 M) was added to ease the precipitate formation.

Photocatalytic hydrogen evolutions. The H$_2$ evolution experiments were accomplished in a 200 ml Pyrex reactor. A UV-LED lamp (25 W, 365 nm, NICHIA, Japan) was used as the light source, which was located 1 cm away from the reactor. Typically, 50 mg of the catalysts were suspended in 200 ml of a 20 vol% aqueous solution of methanol as a sacrificial reagent under sonication. The suspension of photocatalysts was initially purged with argon gas (99.99%) for 30 min (100 mL min^{-1}) to ensure the removal of all oxygen under magnetic stirring. This photocatalytic reaction was performed for 5 h. The amount of H$_2$ produced was measured by gas chromatography (GC-2014, Shimadzu, Japan, with a TCD detector, argon as a carrier gas) every 15 min. The apparent quantum yield (AQY) was measured under similar photocatalytic reaction conditions under various light sources with wavelength of 365, 400, 450, 500, and 520 nm and estimated using the following formula:

$$AQY(\%) = \frac{2 \times \text{the number of evolved H}_2 \text{ molecules}}{\text{the number of incident photons}} \times 100$$

Photocatalytic degradation of MB. The as-prepared photocatalysts were used for the photocatalytic degradation of MB under UV–Vis light irradiation. The light source was a 450 W medium-pressure mercury lamp. The distance between the reaction cell and the light source was approximately 10 cm. First, 50 mg of the photocatalyst was injected into 50 mL of 50 ppm MB aqueous solution. Initially, the suspension was treated

ultrasonically for 30 min and the mixture was stirred magnetically in the dark for 30 min to reach adsorption/desorption equilibrium. The suspension was exposed continuously to light illumination until complete decolorization of the dye solution. At an appropriate interval 4 mL of the suspensions were withdrawn and centrifuged to remove the photocatalyst powder. The concentration of MB was measured using UV–Vis absorption spectra (Lambda-40, Perkin Elmer, USA). The photodegradation of MB dye was also studied under only visible light illumination using the same lamp with a < 420 nm UV cut-off filter (0.72 M $NaNO_2$ solution) in the presence of 5 ml H_2O_2. The degradation efficiency of the as-prepared photocatalysts was calculated using the equation:

$$Removal\ (\%) = (C_o - C_t)/C_o \times 100$$

where, C_o and C_t are the initial concentration of MB and the MB concentration at a specific time, respectively[34].

Photoelectrochemical measurements PEC. Photoelectrochemical experiments were conducted using a three-electrode configuration in which platinum wire, saturated Ag/AgCl electrode, and as-synthesized photocatalysts deposited on a fluorine-doped tin oxide (FTO) conducting glass substrate served as the counter, reference, and working electrodes, respectively. In addition, the used electrolyte was 0.1 M Na_2SO_4 aqueous solution. The light irradiation source equipped was UV-LED lamp (25 W, 365 nm, NVMUR020A, NICHIA, Japan). Prior to the measurement, the electrolyte was bubbled with argon gas to eliminate all dissolved air. To prepare the working electrode, 20 mg of the as-synthesized catalyst was ultra-sonicated with 1 ml of isopropanol to obtain slurry. Subsequently, a 200 µl of the slurry (four layers, 50 µl for each layer) was dropped onto a fixed area of FTO glass 1 cm², and then dried at 100 °C for 1 h.

Electrochemical impedance spectroscopy (EIS), Mott–Schottky (MS) analysis, Chronoamperometry (CAM), and cyclic voltammetry (CV) were measured using a potentiostat workstation (CorrTest Instruments, model CS350) and CS studio software. The EIS spectra were obtained over a frequency range from 100 kHz to 10 mHz. The photocurrent response was implemented at a potential of + 0.6 V vs. Ag/AgCl.

Instrumentation and characterization. The crystallographic phase of the as-synthesized photocatalyst was detected with Philips 1700 version diffractometer (40 kV and 30 mA using Cu Ka radiation), the XRD pattern was acquired in the 2θ range of 4° to 80°. The UV–Vis diffuse reflectance spectra (DRS) were conducted on Evolution 220 spectrophotometer (Thermo Fisher Scientific, UK) in the range of 200–1100 nm. The specific surface areas and porosity of the samples were obtained by N_2 adsorption–desorption isotherm at 77 K using the Brunauer–Emmett–Teller (BET) and Barrett–Joyner–Halenda (BJH) methods (Quantachrome Instrument Corporation, Nova 3200, USA instrument). Prior to surface area analysis, the powders were degassed at 150 °C for 2 h. The morphological characteristics of the as-prepared samples were investigated using transmission electron microscopy (JEOL JEM-2100F). The electrons beam was accelerated to typically 200 kV. The photodegradation rate of MB solution was followed using Lambda-40 UV–Vis spectrophotometer (Perkin Elmer, USA). The chemical composition of the samples was carried out using X-ray photoelectron spectroscopy (XPS, Thermo Scientific, USA, Kα with monochromatic X-ray (Al Kα radiation of − 10 to 1350 eV) with spot size 400 µm, pressure 10^{-9} bar, full-spectrum pass energy 200 eV, and narrow-spectrum 50 eV. The photoluminescence spectra (PL) were probed using Cary Eclipse, Agilent USA fluorescence spectrophotometer.

Results and discussion
Photocatalysts characterization. The crystal structure and composition of the as-prepared samples were analyzed using X-ray diffraction technique. Figure 1 displays the XRD patterns of the pure TiO_2 P25, CuS/TiO_2, and MoS_2/TiO_2 photocatalysts. The diffraction peaks were indexed to TiO_2 p25; the characteristic peaks were located at approximately 25.3°, 37.9°, 48.04°, 54.1°, 55.1°, 62.72°, and 68.99° 2θ were indexed to the (101), (004), (200), (105), (211), (204), and (116) planes of anatase TiO_2 (JCPDS No. 71-1167), respectively. The peak at 27.34° 2θ (110) was assigned to rutile TiO_2[35]. No distinct phase change in TiO_2 was observed. In addition, the as-prepared photocatalysts exhibited negligible diffraction peaks for MoS_2 and CuS, owing to the low loading and the high dispersion of CuS and MoS_2 nanoparticles on the surface of TiO_2[26]. The XRD patterns of CuS and MoS_2 are shown in Fig. S1.

N_2 adsorption–desorption studies were carried out to determine the specific surface area (BET) and the average pore size distribution profiles of the modified photocatalysts. Figure 2a suggests that the curves of the prepared catalysts were attributed to type IV isotherm with a H3 hysteresis loop and relative pressure (P/P_o) in the range of 0.7–1.0, indicating a mesoporous structure (2–50 nm)[36]. TiO_2 had the highest BET specific surface area (162.1 m² g⁻¹). The surface area decreased significantly compared to the as-prepared photocatalyst composites: 36.3, 30, 75.34, and 77.4 m² g⁻¹ for 0.5CT_PP, 0.5CT_HT, 3MT_PP, and 3MT_HT, respectively, as listed in Table 1. This decrement in BET specific surface area may be attributed to the distribution of CuS or MoS_2 particles inside the pores of p25 leading to coverage of external surface area, as reported elsewhere[31].

The adsorption–desorption isotherm of different percent's of CT_PP and MT_HT nanocomposites are shown in Fig. S2. Moreover, the pore size distribution curves of the as-prepared photocatalysts were measured using BJH method (Fig. 2b). It was found that the pore radius of the as-prepared samples increased to a wide range compared to TiO_2 (Table 1). This was due to the coexistence of CuS or MoS_2. Moreover, the total pore volume also increases due to the creation of additional pores that enhance the photocatalytic activity. Table 1 lists the corresponding BET specific surface area, total pore volume, and pore radius.

The morphology and particle size of the as-synthesized CuS/TiO_2 and MoS_2/TiO_2 were measured by TEM, HRTEM and energy-dispersive X-ray spectrometry (EDX) analysis. Figure 3.I displays the TEM image of the 3MT_HT nanocomposite synthesized by the hydrothermal method. Well-distributed dark particles of MoS_2 were observed on the surface of TiO_2 (Fig. 3.I.a). Moreover, the HRTEM image (Fig. 3.I.b) displays the lattice
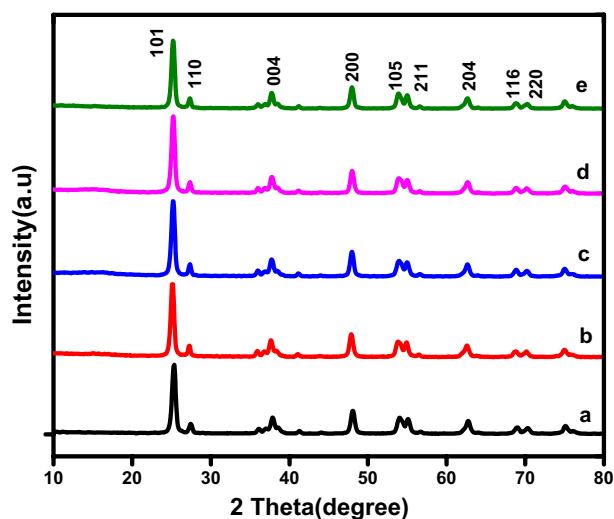
Figure 1. XRD patterns of the as-prepared photocatalysts: (**a**) TiO_2, (**b**) 0.5CT_PP, (**c**) 0.5CT_HT, (**d**) 3MT_HT, and (**e**) 3MT_PP nanocomposites.
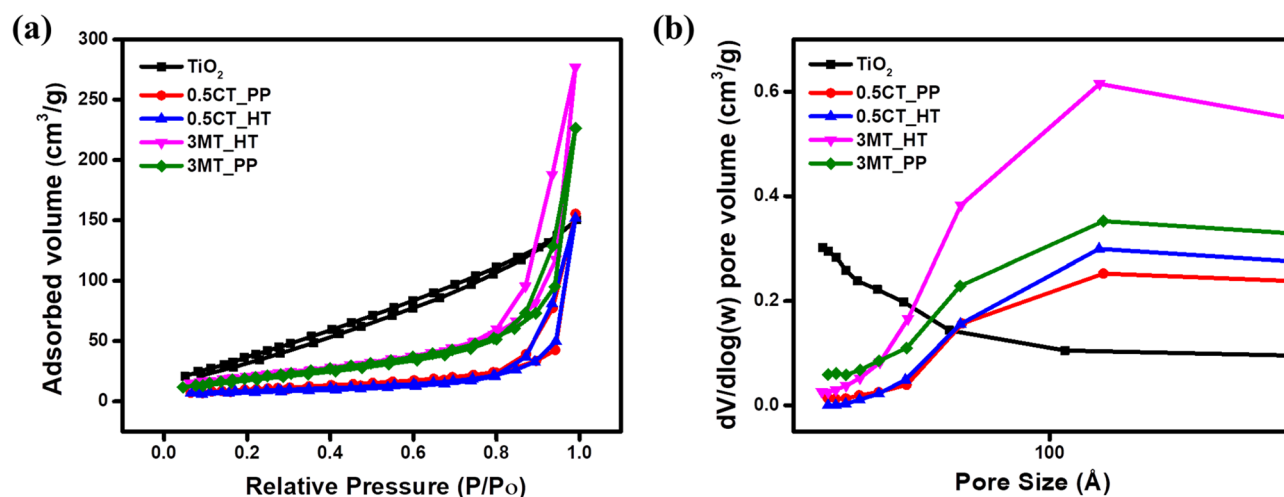

Figure 2. (**a**) N_2 adsorption/desorption isotherm and (**b**) BJH pore size distribution curves of the as prepared photocatalysts.

Samples	S_{BET} (m²/g)	Pore volume (cm³/g)	Pore size (nm)	Band gap (eV)
P25	162.12	0.21	1.58	2.92
0.5CT_PP	36.30	0.23	6.75	2.83
0.5CT_HT	29.99	0.23	11.83	2.22
3MT_PP	75.34	0.34	6.68	1.82
3MT_HT	77.40	0.42	6.71	2.55

Table 1. Summaries of texture properties and optical band gap.

fringe spacing of TiO_2 (0.35 nm) that was attributed to the (101) plane of anatase TiO_2 (JCPDS No. 71-1167)[37]. Whereas, the lattice fringe distance of MoS_2 was 0.62 nm corresponding to (002)[38]. The selected area electron diffraction (SAED) suggests the nanocrystalline nature of the modified photocatalyst. Furthermore, the chemical composition of 3MT_HT heterostructure has been investigated by EDX, which revealed the presence of Ti, O, Mo, and S. On the other hand, the crystal phase corresponding to CuS is hard to be observed in the TEM image of 0.5 CT_PP (Fig. 3.II.a,b). This may be due to the low content and very small CuS particle size. Interestingly, EDX analysis verified the coexistence of Ti, O, Cu, and S. (Fig. 3.II.c).
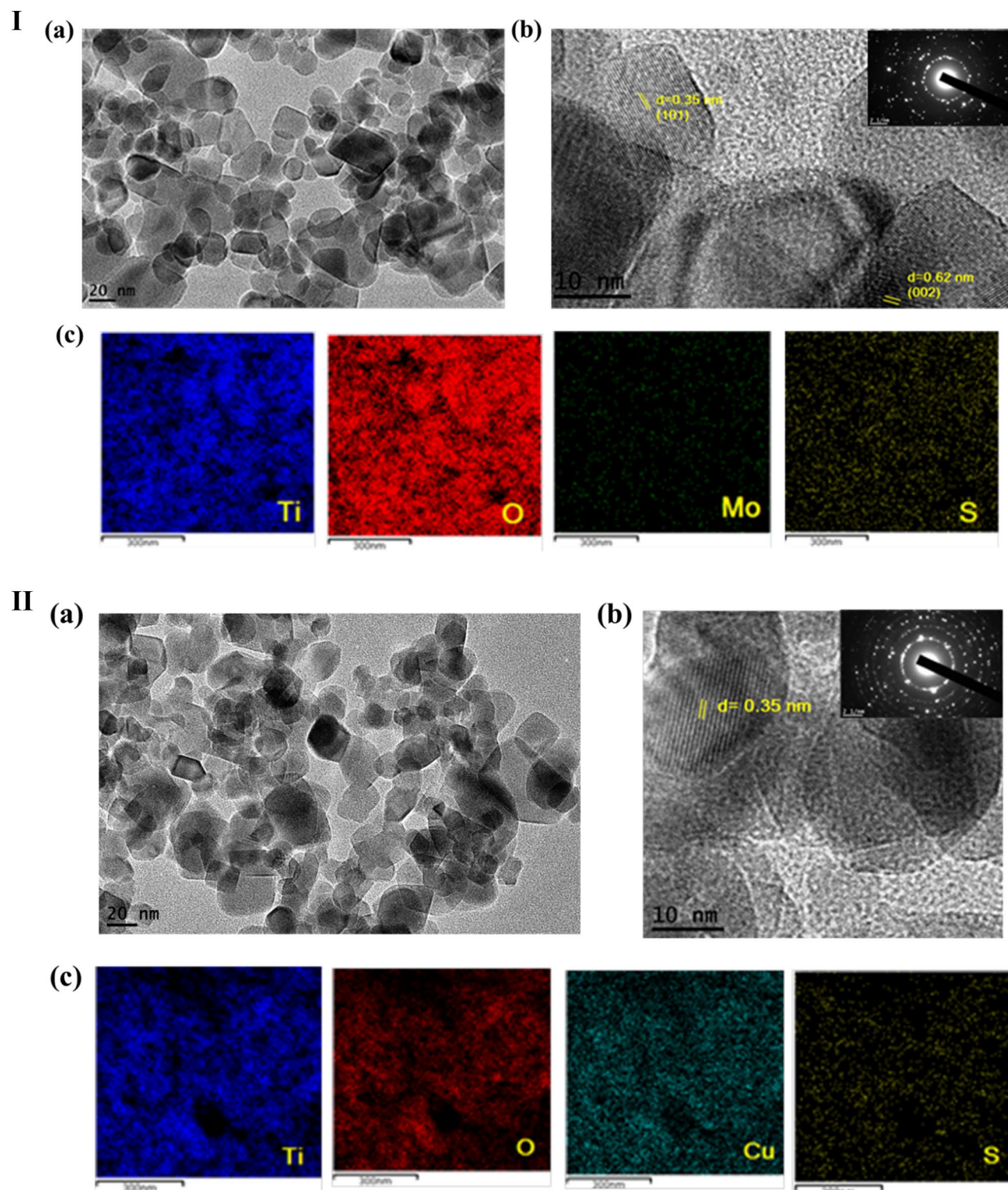
Figure 3. (**I**)—TEM (a), HRTEM image (b) and EDX spectrum (c) of 3MT_HT, respectively. (**II**)—TEM (a), HRTEM image (b) and EDX spectrum (c) of 0.5CT_PP, respectively.

XPS spectra were conducted to identify the composition and chemical state of the 0.5 CT_PP and 3MT_HT nanocomposites. As observed in Fig. 4. The peak at 284.5 could be assigned to C 1s, which was used to calibrate the binding energy positions. The full survey spectrum of the as-prepared 3MT_HT (Fig. 4.I.a) verified the presence of C, Ti, O, Mo, and S elements. As presented in the high resolution XPS spectrum of Ti 2p, the binding energies of Ti $2p_{3/2}$ and Ti $2p_{1/2}$ were situated at 458.9 and 464.7 eV, respectively (Fig. 4.I.b). this indicates the existence of Ti^{4+} oxidation state in the photocatalyst. The Mo 3d HR-XPS spectrum displays the peaks at 231.4 and 234.6 eV, which may be attributed to Mo^{4+} $3d_{5/2}$ and Mo^{4+} $3d_{3/2}$ spin–orbit splitting, respectively. While the
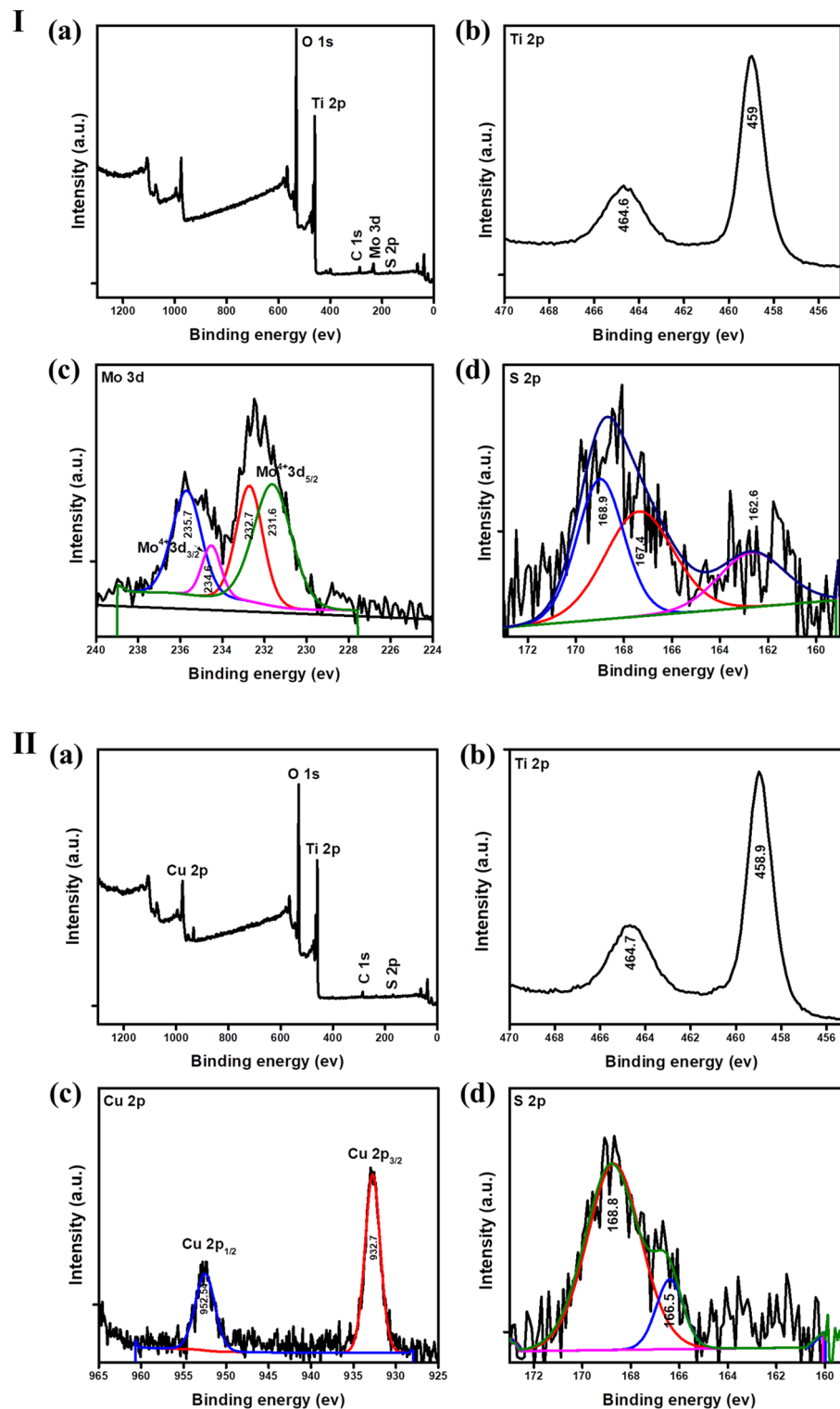
Figure 4.. (**I**) XPS spectrum of the 3MT_HT nanocomposite (a) the full-scale scan, and HR-XPS spectra of (b) Ti 2p, (c), Mo 3d, and (d) S 2p. (**II**) XPS spectrum of the 0.5CT_PP nanocomposite (a) the full-scale scan, and HR-XPS spectra of (b) Ti 2p, (c), Cu 2p, and (d) S 2p.

peaks positioned at 232.7 and 235.7 eV corresponded to Mo^{6+} (Fig. 4.I.c). Furthermore, the peak at 162.6 eV could be corresponded to S $2p_{1/2}$ orbitals of S^{2-}, meanwhile the peaks at 167.4 and 168.4 eV possibly due to the excess of sulfur of MoS_2 on the surface of the as-synthesized photocatalyst (Fig. 4.I.d)[39–42].

The survey spectrum indicated the existence of C, Ti, O, Cu, and S elements in 0.5 CT_PP (Fig. 4.II.a). The two peaks appeared at 458.9 and 464.7 eV were corresponded to Ti $2p_{3/2}$ and Ti $2p_{1/2}$, respectively (Fig. 4.II.b). Furthermore, the Cu 2p high resolution XPS spectrum shows features centered at 932.7 and 952.5 eV, which corresponded to $Cu^{2+} 2p_{3/2}$ and $Cu^{2+} 2p_{1/2}$, respectively (Fig. 4.II.c). The binding energy at 166.5 and 168.8 eV could be ascribed to the S 2p which indicates the existence of S^{2-} this is observed in Fig. 4.II.d[43].

UV/Vis diffuse reflectance analysis was employed to examine the optical properties of the prepared photocatalysts. Figure 5a demonstrates the UV–Vis absorption spectra of TiO_2 and the as prepared CuS/TiO_2 and MoS_2/TiO_2 photocatalysts. It was observed that the pure P25 has absorption at around 390 nm. In the presence of CuS and MoS_2 the absorption edges of the as-synthesized catalysts displaced to higher wavelengths which in turn increase the absorption performance in the visible light region. The photocatalysts showed a noticeable red shift of absorption with increasing the content of CuS, and MoS_2. The UV–Vis absorption spectra different percent's of CT_PP and MT_HT nanocomposites are shown in Fig. S3. The band gap of the as-synthesized samples was estimated using the transformed Kubelka–Munk function (Fig. 5b)[26]. The measured band gap for pure TiO_2 was 2.92 eV. The band gaps of the 0.5CT_PP, 0.5CT_HT, 3MT_PP, and 3MT_HT catalysts were 2.83, 2.22, 1.82, and 2.55 eV, respectively. TiO_2 modified with CuS and MoS_2 is beneficial for electron–hole generation. Suggesting that addition of metal sulfide over TiO_2 surface can increase the optical absorption, as metal sulfides modified TiO_2 nanocomposites could be excited under visible light irradiation and generate additional electron–hole pairs compared to TiO_2, which in turn enhance the photocatalytic activity.

To further investigate the efficiency of the photogenerated electron–hole pair's transformation and recombination process in the as-prepared samples, photoluminescence (PL) analysis was applied. Figure 6a,b show the PL spectra of TiO_2, CT_PP, and MT_HT photocatalysts. A wide emission peak can be observed at around 370 nm. For pure TiO_2, the PL curve intensity is greater than that of the other photocatalysts. Meanwhile, a remarkable decrease in the PL peak intensity of 0.5CT_PP and 3MT_HT was observed. In general, a lower PL intensity indicates higher separation efficiency of the photogenerated carriers. This verifies that modification of TiO_2 with CuS or MoS_2 can reduce the recombination rate of photoexcited carriers. Moreover, the photocatalytic activity can be improved[44].

Photocatalytic H_2 generation activity. The photocatalytic hydrogen evolution experiments of pure TiO_2 and the as-prepared MS_x/TiO_2 nanocomposites with different CuS and MoS_2 contents were performed using an aqueous methanol solution as a scavenger agent and exposure to a UV lamb. It can be seen that pure TiO_2 exhibited a weak HER behavior (0.086 mmol h^{-1} g^{-1}) owing to its large band gap and the fast backward reaction. However, the presence of CuS or MoS_2 led to remarkable growth in the H_2 evolution rate. In the case of CuS/TiO_2 catalysts, the highest activity toward H_2 production was observed for 0.5 wt% CuS/TiO_2 prepared by coprecipitation method with an initial hydrogen evolution rate (HER) 2.95 mmol h^{-1} g^{-1} which was thirty-five times greater than that of pure TiO_2. Although the H_2 production rate of 0.5 CuS/TiO_2 prepared hydrothermally was 2.83 mmol h^{-1} g^{-1}. Furthermore, the maximum H_2 evolution rate of MoS_2/TiO_2 achieved 1.68 mmol h^{-1} g^{-1} when the content of MoS_2 was 3 wt% synthesized by hydrothermal method nearly twenty times as that over pure TiO_2, and it was 1.013 mmol h^{-1} g^{-1} by precipitation method as presented in Fig. 7a. For comparison, different CuS and MoS_2 mass ratios were tested over TiO_2 under the same reaction condition (Fig. 7b,c), respectively. It is observed that increasing the amount of the metal sulfide causes a remarkable decrease in the photocatalytic performance, which is possibly due to the increased shielding of the co-catalyst on the TiO_2 surface, which hinders the electron–hole pair transfer and decreases the exposed active sites[33,45]. The calculated AQY of photocatalytic H_2 production over 0.5CT_PP nanocomposite was ~ 3.2% at 365 nm (Fig. S4). the stability and recyclability tests
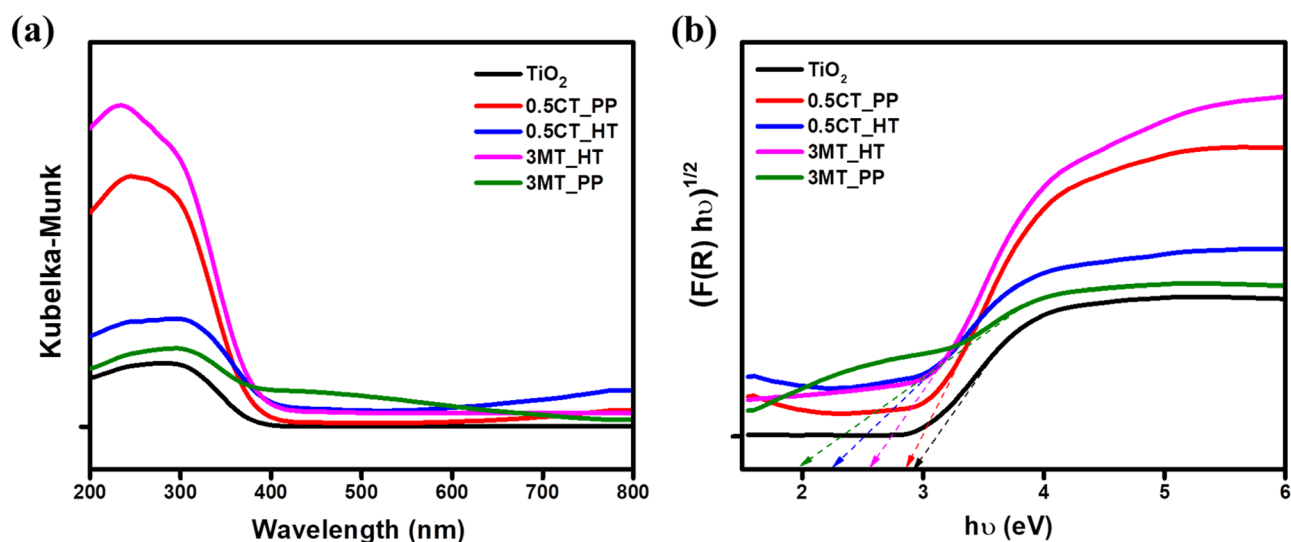

Figure 5. (**a**) UV–Vis absorbance spectra of TiO_2, MoS_2/TiO_2 and CuS/TiO_2 nanocomposites. (**b**) Plots of transformed KM function.
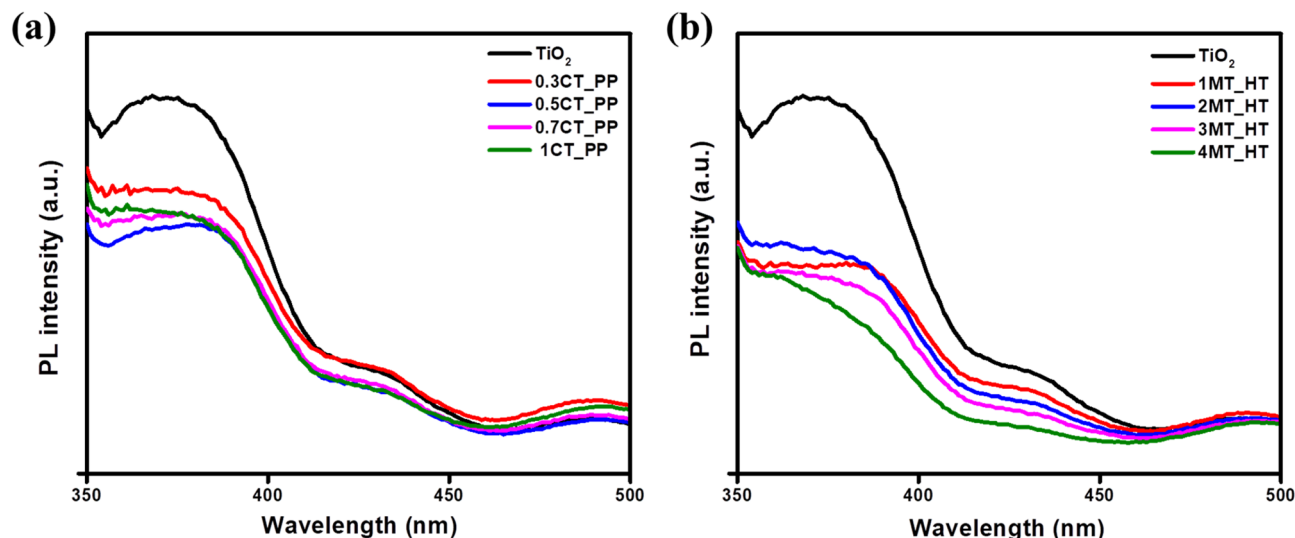
(a)

(b)

Figure 6. Photoluminescence spectra PL of (**a**) CT_PP, and (**b**) MT_HT compared to TiO$_2$.

of 0.5CT_PP and 3MT_HT photocatalysts (100 mg) for H$_2$ generation were performed under UV light (365 nm) for four cycles (20 h). After each cycle the reaction vessel was purged with argon gas for 1 h under dark conditions. As demonstrated in Fig. 7d, the photocatalytic activity of 0.5CT_PP and 3MT_HT remains very stable up to three cycles. Whereas, the catalytic behavior slightly decreased in the 4th cycle, which may be attributed to the consumption of the hole scavenger solution. This suggests that the prepared nanocomposite exhibit excellent stability for photocatalytic hydrogen evolution. Moreover, the XRD analysis of 0.5CT_PP and 3MT_HT before and after recycling tests was carried out. The XRD pattern preserves its original form after the photocatalytic reaction indicating the stability of the crystal structure of the prepared catalysts for long time (Fig. S5). Table 2 shows hydrogen generation rate of the prepared samples and other metal sulfide/TiO$_2$ based photocatalysts.

Photodegradation of MB dye. The photocatalytic performance of CuS/TiO$_2$ and MoS$_2$/TiO$_2$ photocatalysts can also be assessed by the photodegradation of MB solutions under both visible and UV irradiation light using a 450 W medium-pressure mercury lamp with a < 420 nm UV cut-off filter for two hours. First, the synthesized catalysts were exposed to a 50 mg/L MB dye solution for 30 min in the dark conditions to reach adsorption–desorption equilibrium. MoS$_2$/TiO$_2$ nanocomposites had superior efficiency toward MB degradation under visible light (Fig. 8a). After 120 min visible light irradiation, 3MT_HT exhibits a significant photocatalytic performance compared to P25. The appropriate amount of MoS$_2$ has a great influence on enhancing the catalytic activity of TiO$_2$. After exposure to visible light, the degradation efficiency of MB dye over P25 was enhanced from 28.8 to 58.33% over 3MT_PP. The band gap of TiO$_2$ P25 shifted from the UV region (2.93 eV) to the visible region (1.82 eV) on 3MT_PP, as shown in Table 1. A further increase in the photocatalytic activity has observed by the injection of 5 mL H$_2$O$_2$ in the suspension leading to an efficiency of 100% and 99% over 3MT_PP and 3MT_HT after 120 min visible light irradiation (Fig. 8a), respectively. It has been found that CuS/TiO$_2$ nanocomposites had minuscule adsorption ability toward the MB solution compared to P25 (Fig. 8b). For comparison, the photodegradation percentages of MB solution under the visible light irradiation were 19%, 18%, 24.5%, and 25.3%, for p25, 0.3CT_PP, 0.5CT_PP, and 0.5CT_HT, respectively, suggesting that the formation of a heterostructure between CuS and TiO$_2$ can enhance the photocatalytic performance, Among those, 0.5CT_HT shows the highest photocatalytic efficiency because its band gap becomes 2.22 eV (Table. 1). Furthermore, the addition of H$_2$O$_2$ increased the photodegradation , and the removal efficiency reached 93%, and 96% for 0.5CT_PP and 0.5CT_HT, respectively[51]. On the other hand, the photodegradation of MB aqueous solution under the illumination of UV–Vis light is illustrated in Fig. 8c. The results indicate that the photocatalytic activity was improved at 0.5CT_PP and 3MT_HT which rose to nearly 98%, indicating that CuS and MoS$_2$ can form a heterojunction with TiO$_2$, which can, in turn, enhance the photocatalytic activity. The photodegradation of MB by MS/TiO$_2$ based photocatalysts are summarized in Table 3.

To investigate the contribution of active species during the photocatalytic degradation of MB, elemental trapping experiments have been performed in which, isopropanol (IPA), p-benzoquinone (BQ) and ethylene diamine tetraacetic acid disodium (EDTA-2Na) were used as scavengers to quench the free radical hydroxide ·OH, superoxide radical ·O$_2^-$ and photogenerated holes h$^+$, respectively. As shown in Fig. 8d, the photodegradation of MB over 3MT_HT without any scavenger reached 98% under UV–Vis irradiation for 2 h. The addition of IPA decreased the activity to 48.2%, while the degradation efficiency quenched to 87.8 and 78% when using p-BQ and EDTA-2Na, respectively. These results indicate that ·OH radical is the major active species for the dye degradation reaction. However, h$^+$ and ·O$_2^-$ have a minor effect on the photocatalytic process. The effect of catalyst amount and the initial pH of the solution are presented in Fig. S6. The pH of the solution was adjusted using diluted HCl solution and diluted NaOH solution.
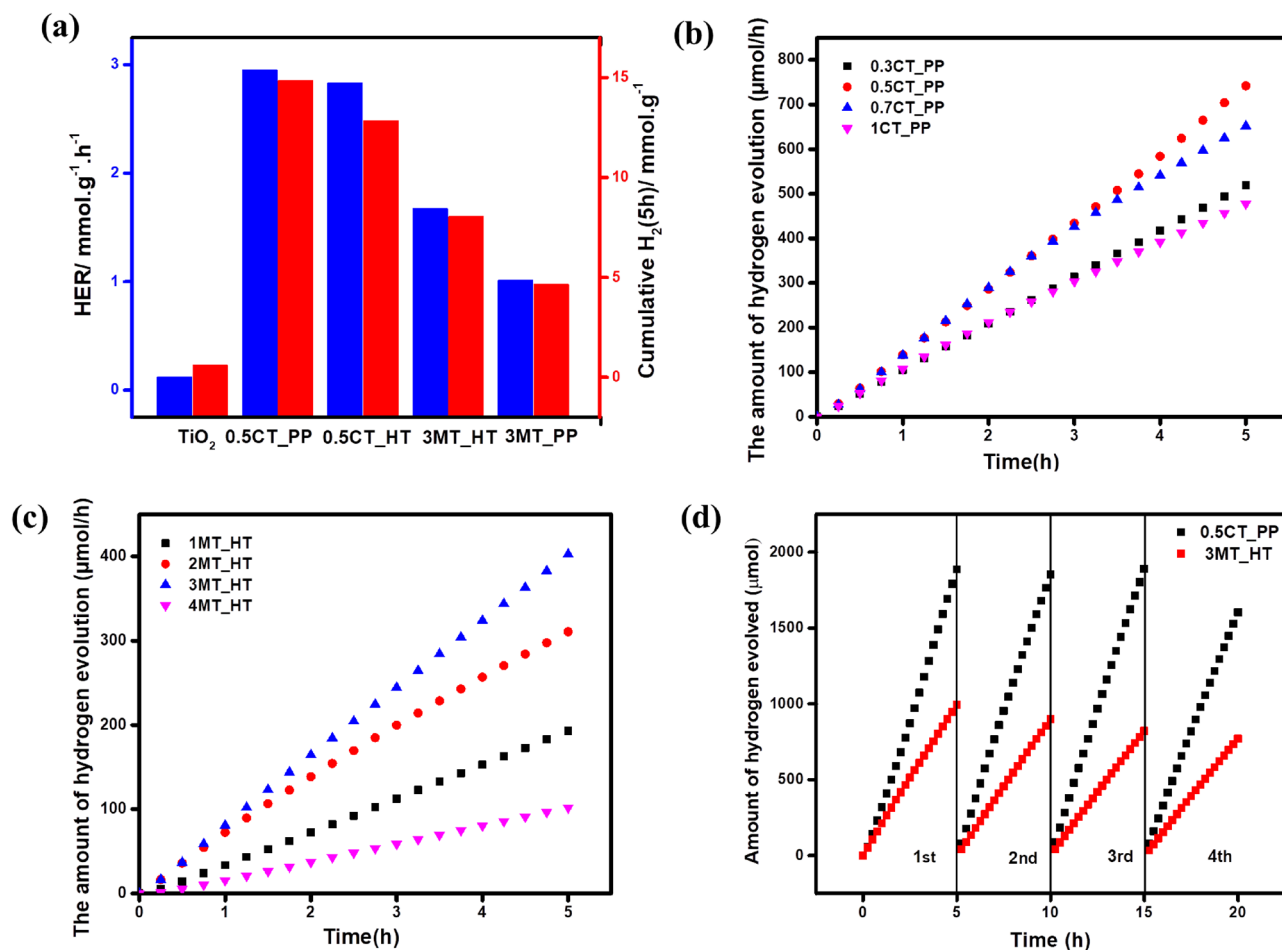
Figure 7. (**a**) The initial and cumulative (5 h) hydrogen evolution rate. (**b,c**) Time course of H_2 evolution over of different weight percent of CuS/TiO_2 and MoS_2/TiO_2, respectively, and (**d**) Recycling test of H_2 evolution over 0.5CT_PP and 3MT_HT photocatalysts.

Photoelectrochemical measurements. Electrochemical measurements using EIS, CAM, and CV were carried out to validate the improved separation efficiency of the electron–hole pair in metal sulfides modified TiO_2 nanocomposite[57]. The transient photocurrent responses of the as-prepared electrodes were measured under UV light irradiation at a bias potential of 0.6 V (vs. Ag/AgCl). In a 0.1 M Na_2SO_4 electrolyte solution. The photocurrent response increased immediately as the light was turned on and decreased to zero after turning off the light. The photocurrents of 0.5CT_PP, 0.5CT_HT, 3MT_HT and 3MT_PP were better than pristine TiO_2, as shown in Fig. 9a. The 0.5CT_PP and 3MT_HT nanocomposites were 22 and 12 times higher than that of

Photocatalysts	Synthesis method	Sacrificial reagent	Light source	Activity μmol h^{-1} g^{-1}	Ref
MoS_2/TiO_2	In-situ photo-deposition	Triethanolamine	1000 W Xe arc lamp	ca. 1630	[46]
MoS_2 nanosheets/TiO_2 nanosheets	Hydrothermal	10 vol% methanol/H_2O	300 W Xe lamp	2145	[47]
CuS nanoflakes/TiO_2 nano-spindles	Chemical precipitation	0.35 M Na_2S and 0.25 M Na_2SO_3	300 W Xe lamp ($\lambda > 420$ nm)	1262	[29]
CuS nanoflowers/TiO_2 NPs/ Pt NPs	Hydrothermal	0.1 m Na_2S + 0.1 m Na_2SO_3	400 W Xe lamp ($\lambda > 395$ nm)	746	[48]
Ag-Ag_2S NPs/TiO_2 NPs	In situ sulfidation of Ag	10 v% methanol/H_2O	4 LEDs (3 W, 365 nm, 80.0 mW cm^{-2})	2382.2	[49]
CoSx quantum dots/TiO_2	Deposition–precipitation	20 vol% ethanol	300WXe lamp	838	[50]
0.5CT_PP	Precipitation	20 vol% methanol	UV-LEDs	2950	This work
3MT_HT	Hydrothermal	20 vol% methanol	UV-LEDs	1700	This work

Table 2. Comparison table on hydrogen generation performance of 0.5CT_PP and 3MT_HT with other transition metal sulfides/TiO_2 based photocatalysts.
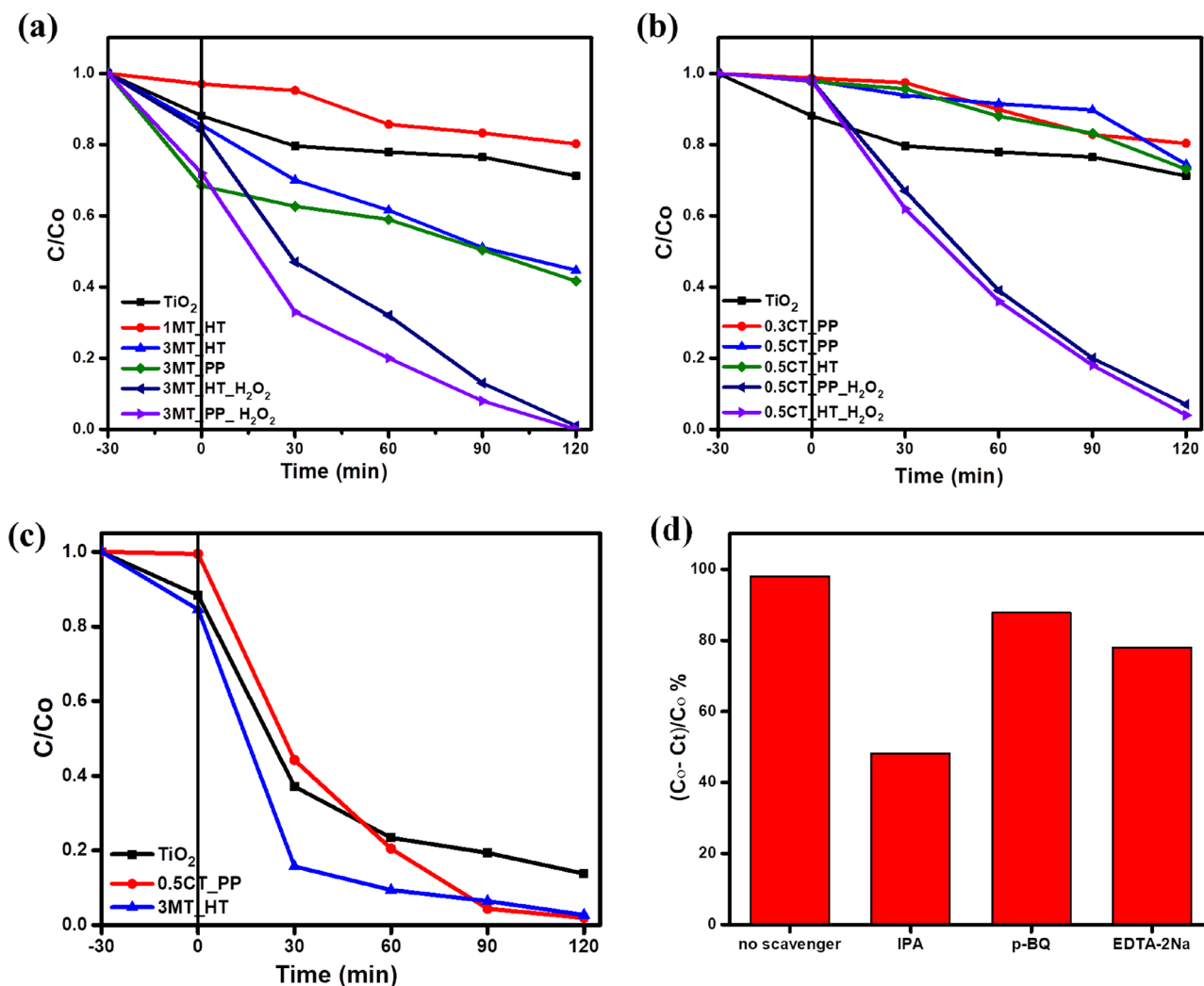
Figure 8. Photodegradation of MB of TiO$_2$ and different percent's of (**a**) MoS$_2$/TiO$_2$, (**b**) CuS/TiO$_2$ with and without H$_2$O$_2$ under visible light. (**c**) Photodegradation behavior of MB of TiO$_2$, 0.5CT_PP, and 3MT_HT under UV–Vis light. (**d**) Trapping experiments of active species over 3MT_HT (pH 6.5, 50 mg of catalyst, 50 ppm MB).

Photocatalysts	Synthesis method	Pollutant content/(mg L^{-1})	Light Source	% of degradation	Ref
MoS$_2$/TiO$_2$	Hydrothermal method	5 mg/L	400 W Xe lamp visible light	99.33	[52]
Cu$_x$S/TiO$_2$	In situ synthesis	10 mg/L	Visible	95	[53]
CdS/TiO$_2$	SILAR method	12 mg/L	160 W Hg lamp	93.8	[54]
PbS/GR/TiO$_2$	Sol–gel method	1×10^{-4} M	Visible	41	[55]
CuS/TiO$_2$ nanofiber	Electrospinning and hydrothermal processes	10 mg/L	Visible	79.09	[56]
0.5CT_HT	Hydrothermal	50 mg/L MB + H$_2$O$_2$	450 W Hg lamp visible light	96	This work
3MT_PP	Precipitation	50 mg/L MB + H$_2$O$_2$	450 W Hg lamp visible light	100	This work

Table 3. Comparison table on photodegradation of MB of the as-prepared photocatalysts with metal sulfides modified TiO$_2$.

pure TiO$_2$, respectively. Hence, heterojunction formation between metal sulfides and TiO$_2$ leads to enhanced charge separation. Moreover, the photocurrent response exhibited reproducibility, representing the high stability of the as-prepared photocatalysts. Figure 9b displays the EIS Nyquist plots of TiO$_2$, 0.5CT_PP, 0.5CT_HT, 3MT_HT, and 3MT_PP under UV light irradiation. EIS was used to study the charge separation efficiency. The semi-circle refers to the charge transfer resistance across the interface. Impedance fitting revealed a significantly reduced semi-circle of 0.5CT_PP, indicating that 0.5CT_PP has a significantly improved charge transfer efficiency, enhanced conductivity, and superior separation of photogenerated charges, resulting in an improved
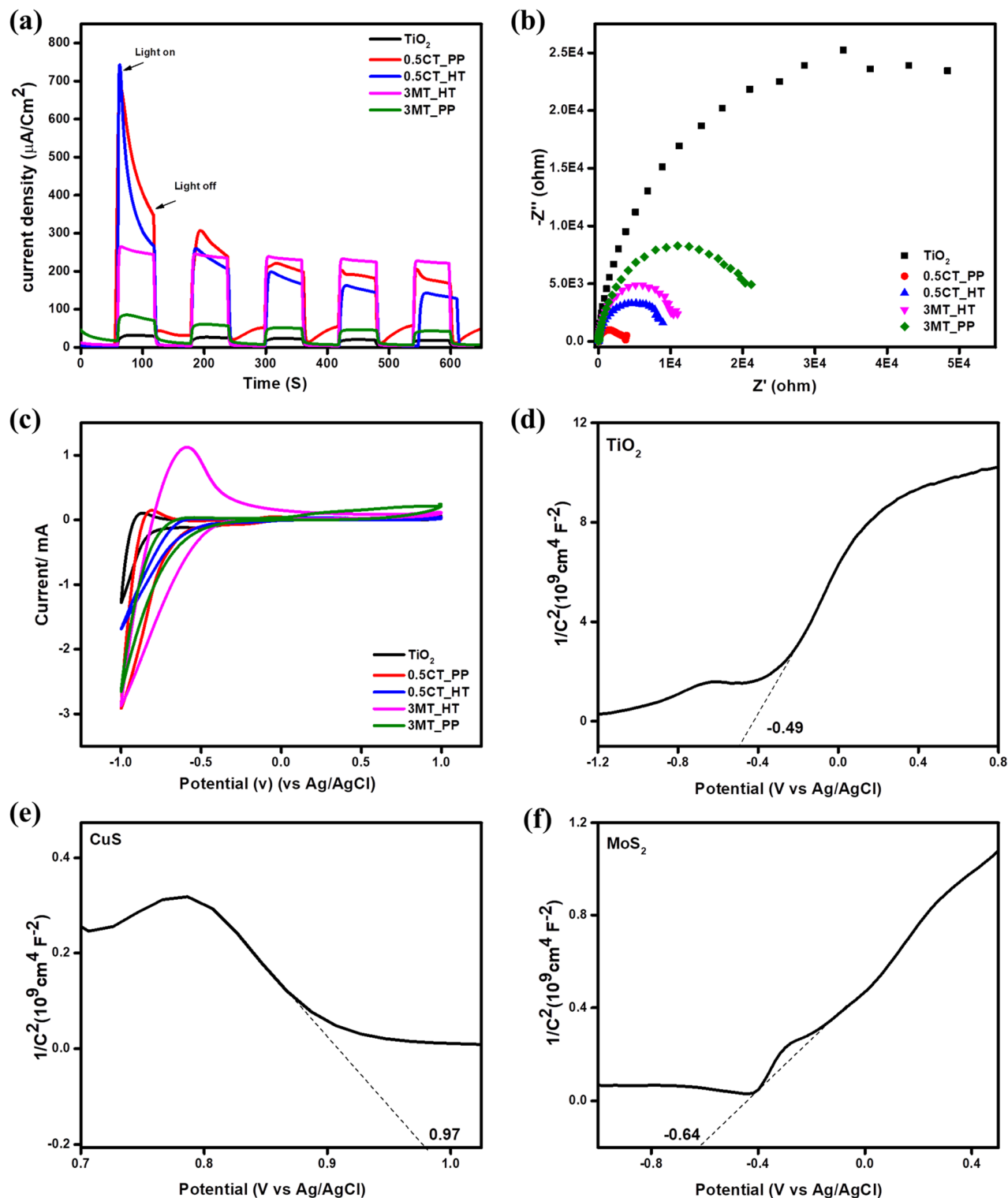
Figure 9. (**a**) Transient photocurrent response (i–t); (**b**) EIS Nyquist plots, (**c**) cyclic voltammetry curves of TiO_2, 0.5CT_PP, 0.5CT_HT, 3MT_HT and 3MT_PP photocatalysts, Mott–Schottky plots of pure (**d**) TiO_2, (**e**) CuS, and (**f**) MoS_2.

photocatalytic performance of the as-synthesized photocatalysts than that of pure TiO_2. Furthermore, CV was performed to estimate the catalytic performance and the reduction sites of the prepared metal sulfide/TiO_2 catalysts. The estimated reduction currents for TiO_2, 0.5CT_PP, 0.5CT_HT, 3MT_HT and 3MT_PP were 1.30, 2.94, 1.71, 2.90, and 2.66 mA cm^{-2}, respectively (Fig. 9c), indicating that the cathodic current has been improved.

Mott–Schottky (MS) analysis was used to investigate the conductivity and flat band potentials (E_{FB}) of pure CuS, MoS_2, and TiO_2[58]. TiO_2 and MoS_2 are n-type semiconductors while CuS is a p-type semiconductor

(Fig. 9d–f). The measured (E_{FB}) for TiO$_2$, MoS$_2$ and CuS were -0.49, -0.64 and 0.97 V *vs.* Ag/AgCl, respectively. These values can be transformed to the normal hydrogen electrode (NHE) scale using the following equation: $E_{NHE} = E_{Ag/AgCl} + 0.197$.

Photocatalytic mechanism. In the light of the previous discussion, the possible mechanism for H$_2$ generation and MB degradation over the as-prepared metal sulfides doped TiO$_2$ photocatalysts is shown in Fig. 10. Under light illumination, TiO$_2$ modified by CuS or MoS$_2$ was excited, leading to the generation of charge carriers. The photoexcited electrons on the CB of CuS or MoS$_2$ could transfer directly to the CB of the TiO$_2$, because the CB edge potentials of CuS (-0.71) and MoS$_2$ (-0.64) are more negative than TiO$_2$ (-0.49). Meanwhile, the VB level of TiO$_2$ (2.51) is more positive than that of CuS (1.37) and MoS$_2$ (0.96), thus the photoexcited holes migrate in the reverse direction of electrons. The band gaps of CuS and MoS$_2$ are displayed in Fig. S7a,b. Based on the band alignment data, the heterojunction between the metal sulfide and TiO$_2$ follow type II. This could be further verified via elemental trapping experiments in the MB degradation. It was found that the primary active species is the free radical hydroxide ·OH for the photodegradation reaction. Whereas, superoxide radical ·O$_2^-$ was minor active species and didn't contribute sufficiently in the photodegradation of MB[59,60]. On the other hand, under UV irradiation, photogenerated electrons produced by metal sulfides could transfer to the surface of TiO$_2$ resulting in the reduction of 2H$^+$ to H$_2$, while the photogenerated holes react with methanol. The photodegradation of MB under UV–Vis and only Vis light irradiation involves the capture of the photogenerated electrons accumulated on the CB of TiO$_2$ by an O$_2$ molecule to produce ·O$_2^-$. In the presence of H$_2$O$_2$, it can interact to generate ·OH to degrade MB. Meanwhile, the photogenerated holes accumulated in the VB of CuS and MoS$_2$ react with OH$^-$ and adsorbed organics to produce ·OH. Bare wide band gap TiO$_2$ has poor photocatalytic activity due to the high recombination rate of electron–hole pairs and crystal defects. Loading of metal sulfide on the surface of TiO$_2$ could improve the interfacial charge transfer, suppress charge recombination, and inhibit the backward reaction. This in turn causes a substantial increase in the catalytic performance toward both H$_2$ evolution and dye degradation[1,61].

Conclusion

In summary, CuS/TiO$_2$ and MoS$_2$/TiO$_2$ photocatalysts have been successfully synthesized by facile coprecipitation and hydrothermal method with different weight percent's, which exhibited a superior photocatalytic activity toward H$_2$ generation and MB degradation compared to TiO$_2$. Various techniques were used to characterize the as-prepared catalysts. The optimal CuS loading content to TiO$_2$ was 0.5wt% prepared by coprecipitation method with a hydrogen evolution rate of 2.95 mmol h^{-1} g^{-1} and the degradation efficiency of MB was 93% in the presence of H$_2$O$_2$ under visible light. Meanwhile, the maximum photocatalytic hydrogen production rate of TiO$_2$ modified with MoS$_2$ was achieved by 3MT_HT (1.7 mmol h^{-1} g^{-1}) and the photodegradation of MB was 99%. To further investigate the superior charge carrier transfer and the photocatalytic activity of 0.5CT_PP and 3MT_HT, photoelectrochemical measurements (PEC) were undertaken. Under light irradiation (365 nm), from EIS study, the Nyquist plots of the samples show that 0.5CT_PP had the smallest semicircle arc indicating the highest charge carrier separation and excellent charge transport characteristics. This plays a crucial role in enhancement its photocatalytic activity for hydrogen generation. Also, the photocatalytic activity can be evaluated using cyclic voltammetry (CV) measurements, where 0.5CT_PP had the highest cathodic current which indicates that TiO$_2$ loaded by 0.5 wt% CuS prepared via co-precipitation method has the greatest photocatalytic H$_2$ performance.
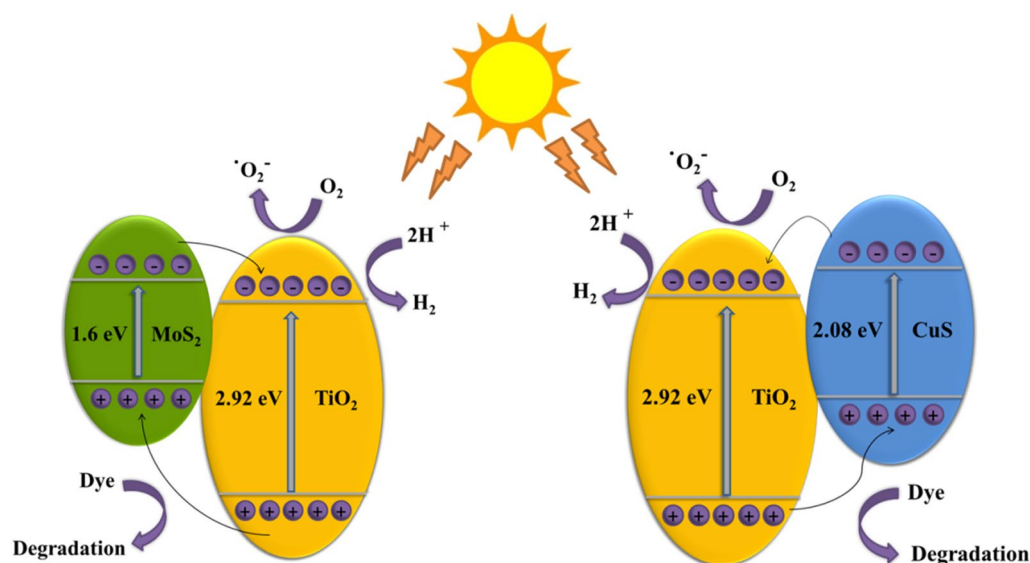

Figure 10. Scheme illustrating the photocatalytic mechanism of CuS/TiO$_2$ and MoS$_2$/TiO$_2$.

In conclusion, coupling of metal sulfides with TiO_2 enhances the separation of the photoinduced electrons and holes, which in turn improve the photocatalytic performance.

Data availability

All data generated or analyzed during this study are included in this published article (and its supplementary information files).

References

1. Klara, P. *et al.* Recent achievements in development of TiO_2-based composite photocatalytic materials for solar driven water purification and water splitting. *Materials* **13**, 1338 (2020).
2. Ran, J., Zhang, J., Yu, J., Jaroniec, M. & Qiao, S. Z. Earth-abundant cocatalysts for semiconductor-based photocatalytic water splitting. *Chem. Soc. Rev.* **43**, 7787–7812 (2014).
3. Farrag, M. Monodisperse and polydisperse platinum nanoclusters supported over TiO_2 anatase as catalysts for catalytic oxidation of styrene. *J. Mol. Catal. A Chem.* **413**, 67–76 (2016).
4. Fujishima, A. & Honda, K. Electrochemical photolysis of water at a semiconductor electrode. *Nature* **238**, 37–38 (1972).
5. Kudo, A. & Miseki, Y. Heterogeneous photocatalyst materials for water splitting. *Chem. Soc. Rev.* **38**, 253–278 (2009).
6. Meng, A., Zhang, L., Cheng, B. & Yu, J. Dual cocatalysts in TiO_2 photocatalysis. *Adv. Mater.* **31**, 1807660 (2019).
7. Nabil, S., Hammad, A. S., El-Bery, H. M., Shalaby, E. A. & El-Shazly, A. H. The CO_2 photoconversion over reduced graphene oxide based on Ag/TiO_2 photocatalyst in an advanced meso-scale continuous-flow photochemical reactor. *Environ. Sci. Pollut. Res.* **28**, 36157–36173 (2021).
8. Farrag, M. & Yahya, R. Selective solar photocatalytic oxidation of benzyl alcohol to benzaldehyde over monodispersed Cu nanoclusters/TiO_2/activated carbon nanocomposite. *J. Photochem. Photobiol. A Chem.* **396**, 112527 (2020).
9. Nakata, K. & Fujishima, A. TiO_2 photocatalysis: Design and applications. *J. Photochem. Photobiol. C Photochem. Rev.* **13**, 169–189 (2012).
10. Saleh, M. R., Ahmed, S. M., Soliman, S. A. & El-Bery, H. M. Facile construction of self-assembled Cu@polyaniline nanocomposite as an efficient noble-metal free cocatalyst for boosting photocatalytic hydrogen production. *Int. J. Hydrogen Energy* **47**, 6011–6028 (2022).
11. Mohamed, O. S., Ahmed, S. A., Mostafa, M. F. & Abdel-Wahab, A. M. A. Nanoparticles TiO_2-photocatalyzed oxidation of selected cyclohexyl alcohols. *J. Photochem. Photobiol. A Chem.* **200**, 209–215 (2008).
12. El-Bery, H. M., Salah, M. R., Ahmed, S. M. & Soliman, S. A. Efficient non-metal based conducting polymers for photocatalytic hydrogen production: Comparative study between polyaniline, polypyrrole and PEDOT. *RSC Adv.* **11**, 13229–13244 (2021).
13. Shuang, S., Lv, R., Xie, Z. & Zhang, Z. Surface plasmon enhanced photocatalysis of Au/Pt-decorated TiO_2 nanopillar arrays. *Sci. Rep.* **6**, 26670 (2016).
14. Melvin, A. A. *et al.* M-Au/TiO_2 (M = Ag, Pd, and Pt) nanophotocatalyst for overall solar water splitting: Role of interfaces. *Nanoscale* **7**, 13477–13488 (2015).
15. Shiraishi, Y., Sakamoto, H., Sugano, Y., Ichikawa, S. & Hirai, T. Pt-Cu bimetallic alloy nanoparticles supported on anatase TiO_2: Highly active catalysts for aerobic oxidation driven by visible light. *ACS Nano* **7**, 9287–9297 (2013).
16. Simon, T. *et al.* Redox shuttle mechanism enhances photocatalytic H_2 generation on Ni-decorated CdS nanorods. *Nat. Mater.* **13**, 1013–1018 (2014).
17. Meng, A., Zhang, J., Xu, D., Cheng, B. & Yu, J. Enhanced photocatalytic H_2-production activity of anatase TiO_2 nanosheet by selectively depositing dual-cocatalysts on (101) and (001) facets. *Appl. Catal. B Environ.* **198**, 286–294 (2016).
18. Yu, X. *et al.* NiO-TiO_2 p-n heterostructured nanocables bridged by zero-bandgap rGO for highly efficient photocatalytic water splitting. *Nano Energy* **16**, 207–217 (2015).
19. Abe, R., Sayama, K. & Arakawa, H. Efficient hydrogen evolution from aqueous mixture of I- and acetonitrile using a merocyanine dye-sensitized Pt/TiO_2 photocatalyst under visible light irradiation. *Chem. Phys. Lett.* **362**, 441–444 (2002).
20. Li, J., Liu, X., Sun, Z. & Pan, L. Novel Bi_2MoO_6/TiO_2 heterostructure microspheres for degradation of benzene series compound under visible light irradiation. *J. Colloid Interface Sci.* **463**, 145–153 (2016).
21. Liu, C. *et al.* A novel Bi_2S_3 nanowire @ TiO_2 nanorod heterogeneous nanostructure for photoelectrochemical hydrogen generation. *Chem. Eng. J.* **302**, 717–724 (2016).
22. Yu, J., Qi, L. & Jaroniec, M. Hydrogen production by photocatalytic water splitting over Pt/TiO_2 nanosheets with exposed (001) facets. *J. Phys. Chem. C* **114**, 13118–13125 (2010).
23. Yu, H., Liu, R., Wang, X., Wang, P. & Yu, J. Enhanced visible-light photocatalytic activity of Bi_2WO_6 nanoparticles by Ag_2O cocatalyst. *Appl. Catal. B Environ.* **111–112**, 326–333 (2012).
24. Tian, J. *et al.* RuO_2/TiO_2 nanobelt heterostructures with enhanced photocatalytic activity and gas-phase selective oxidation of benzyl alcohol. *Sol. Energy Mater. Sol. Cells* **151**, 7–13 (2016).
25. Luo, L. *et al.* Effective visible-light-driven photocatalytic degradation of 17A-ethynylestradiol by crosslinked CdS nano-rod/TiO_2 (B) nano-belt composite. *Process Saf. Environ. Prot.* **130**, 77–85 (2019).
26. Jiang, Y., Zhang, M., Xin, Y., Chai, C. & Chen, Q. Construction of immobilized CuS/TiO2 nanobelts heterojunction photocatalyst for photocatalytic degradation of enrofloxacin: Synthesis, characterization, influencing factors and mechanism insight. *J. Chem. Technol. Biotechnol.* **94**, 2219–2228 (2019).
27. Du, J. *et al.* Highly efficient hydrogen evolution catalysis based on MoS_2/CdS/TiO_2 porous composites. *Int. J. Hydrogen Energy* **43**, 9307–9315 (2018).
28. Hao, X. *et al.* Zn-vacancy mediated electron-hole separation in ZnS/g-C3N4 heterojunction for efficient visible-light photocatalytic hydrogen production. *Appl. Catal. B Environ.* **229**, 41–51 (2018).
29. Chandra, M., Bhunia, K. & Pradhan, D. Controlled synthesis of CuS/TiO_2 heterostructured nanocomposites for enhanced photocatalytic hydrogen generation through water splitting. 2–11 (2018) https://doi.org/10.1021/acs.inorgchem.8b00283.
30. Yin, X. L. *et al.* MoS_2/CdS nanosheets-on-nanorod heterostructure for highly efficient photocatalytic H_2 generation under visible light irradiation. *ACS Appl. Mater. Interfaces* **8**, 15258–15266 (2016).
31. Lin, Y., Ren, P. & Wei, C. Fabrication of MoS_2/TiO_2 heterostructures with enhanced photocatalytic activity. *CrystEngComm* **21**, 3439–3450 (2019).
32. Chen, B. *et al.* Preparation of MoS_2/TiO_2 based nanocomposites for photocatalysis and rechargeable batteries: Progress, challenges, and perspective. *Nanoscale* **10**, 34–68 (2018).
33. Wang, Q. *et al.* CuS, NiS as co-catalyst for enhanced photocatalytic hydrogen evolution over TiO_2. *Int. J. Hydrogen Energy* **39**, 13421–13428 (2014).

34. El-Bery, H. M., Saleh, M., El-Gendy, R. A., Saleh, M. R. & Thabet, S. M. High adsorption capacity of phenol and methylene blue using activated carbon derived from lignocellulosic agriculture wastes. *Sci. Rep.* **12**, 1–17 (2022).

35. Wadhai, S., Jadhav, Y. & Thakur, P. Synthesis of metal-free phosphorus doped graphitic carbon nitride-P25 (TiO_2) composite: Characterization, cyclic voltammetry and photocatalytic hydrogen evolution. *Sol. Energy Mater. Sol. Cells* **223**, 110958 (2021).

36. Sing, K. S. W. *et al.* Reporting physisorption data for gas/solid systems with special reference to the determination of surface area and porosity. *Pure Appl. Chem.* **57**, 603–619 (1985).

37. Yu, B. *et al.* Construction of hollow TiO_2/CuS nanoboxes for boosting full-spectrum driven photocatalytic hydrogen evolution and environmental remediation. 1–10 (2020) https://doi.org/10.1016/j.ceramint.2020.12.006.

38. Huang, Y., Liu, L., Zhao, W. & Chen, Y. Preparation and characterization of molybdenum disulfide films obtained by one-step atomic layer deposition method. *Thin Solid Films* **624**, 101–105 (2017).

39. Wang, B. *et al.* The bimetallic iron–nickel sulfide modified g-C3N4 nano-heterojunction and its photocatalytic hydrogen production enhancement. *J. Alloys Compd.* **766**, 421–428 (2018).

40. Ou, W. *et al.* Two-dimensional ultrathin MoS_2-modified black Ti^{3+}–TiO_2 nanotubes for enhanced photocatalytic water splitting hydrogen production. *J. Energy Chem.* **43**, 188–194 (2020).

41. Kite, S. V. *et al.* Nanostructured TiO_2 sensitized with MoS_2 nanoflowers for enhanced photodegradation efficiency toward methyl orange. *ACS Omega* **6**, 17071–17085 (2021).

42. Abd El-Aal, M., Saleh, M. R. & El-Bery, H. M. Rational design of 1D $NiMoO_4$/0D CdS heterostructures for efficient photocatalytic hydrogen generation under visible light. *Sustain. Energy Fuels* **6**, 3371–3382 (2022).

43. Chang, C. J., Weng, H. T. & Chang, C. C. CuS–$ZnS_{1−x}O_x$/g-C3N4 heterostructured photocatalysts for efficient photocatalytic hydrogen production. *Int. J. Hydrogen Energy* **42**, 23568–23577 (2017).

44. Pei, Z., Weng, S. & Liu, P. Enhanced photocatalytic activity by bulk trapping and spatial separation of charge carriers: A case study of defect and facet mediated TiO_2. *Appl. Catal. B Environ.* **180**, 463–470 (2016).

45. Saleh, M. R. & El-Bery, H. M. Unraveling novel Cu/CuxP@N-doped C composite as effective cocatalyst for photocatalytic hydrogen production under UV and visible irradiation. *Appl. Surf. Sci.* **580**, 152280 (2022).

46. Malekshoar, G. & Ray, A. K. In-situ grown molybdenum sulfide on TiO_2 for dye-sensitized solar photocatalytic hydrogen generation. *Chem. Eng. Sci.* **152**, 35–44 (2016).

47. Yuan, Y. J. *et al.* Constructing anatase TiO_2 nanosheets with exposed (001) facets/layered MoS_2 two-dimensional nanojunctions for enhanced solar hydrogen generation. *ACS Catal.* **6**, 532–541 (2016).

48. Manjunath, K. *et al.* Superior activity of the CuS-TiO_2/Pt hybrid nanostructure towards visible light induced hydrogen production. *New J. Chem.* **40**, 10172–10180 (2016).

49. Yu, H., Liu, W., Wang, X. & Wang, F. Promoting the interfacial H_2-evolution reaction of metallic Ag by Ag_2S cocatalyst: A case study of TiO_2/Ag-Ag_2S photocatalyst. *Appl. Catal. B Environ.* **225**, 415–423 (2018).

50. Li, Y., Yu, Z., Meng, J., Xiao, J. & Li, Y. Cobalt sulfide quantum dots modified TiO_2 nanoparticles for efficient photocatalytic hydrogen evolution. *Int. J. Hydrogen Energy* **39**, 15387–15393 (2014).

51. Wang, Y., Zhang, L., Jiu, H., Li, N. & Sun, Y. Depositing of CuS nanocrystals upon the graphene scaffold and their photocatalytic activities. *Appl. Surf. Sci.* **303**, 54–60 (2014).

52. Sabarinathan, M. *et al.* Highly efficient visible-light photocatalytic activity of MoS_2-TiO_2 mixtures hybrid photocatalyst and functional properties. *RSC Adv.* **7**, 24754–24763 (2017).

53. Gao, L., Du, J. & Ma, T. Cysteine-assisted synthesis of CuS-TiO_2 composites with enhanced photocatalytic activity. *Ceram. Int.* **43**, 9559–9563 (2017).

54. Yang, X. *et al.* Preparation of CdS/TiO_2 nanotube arrays and the enhanced photocatalytic property. *Ceram. Int.* **42**, 7192–7202 (2016).

55. Ullah, K., Meng, Z. D., Ye, S., Zhu, L. & Oh, W. C. Synthesis and characterization of novel PbS-graphene/TiO_2 composite with enhanced photocatalytic activity. *J. Ind. Eng. Chem.* **20**, 1035–1042 (2014).

56. Hou, G. *et al.* Controllable synthesis of CuS decorated TiO_2 nanofibers for enhanced photocatalysis. *CrystEngComm* **17**, 5496–5501 (2015).

57. Saleh, M. R., Thabet, S. M., El-Gendy, R. A., Saleh, M. & El-Bery, H. M. MIL-53 (Fe) for constructing hydrogenated Fe_3O_4@C@TiO_2 double core-shell nanocrystals as superior bifunctional photocatalyst. *J. Photochem. Photobiol. A Chem.* **432**, 114125 (2022).

58. El-Bery, H. M. & Abdelhamid, H. N. Photocatalytic hydrogen generation via water splitting using ZIF-67 derived Co_3O_4@C/TiO_2. *J. Environ. Chem. Eng.* **9**, 105702 (2021).

59. Palanivel, B. & Mani, A. Conversion of a type-II to a Z-scheme heterojunction by intercalation of a 0D electron mediator between the integrative $NiFe_2O_4$/g-C3N4 composite nanoparticles: Boosting the radical production for photo-fenton degradation. *ACS Omega* **5**, 19747–19759 (2020).

60. Ghattavi, S. & Nezamzadeh-Ejhieh, A. A visible light driven AgBr/g-C3N4 photocatalyst composite in methyl orange photodegradation: Focus on photoluminescence, mole ratio, synthesis method of g-C3N4 and scavengers. *Compos. Part B Eng.* **183**, 107712 (2020).

61. Lu, Y. Y. *et al.* In situ loading of CuS nanoflowers on rutile TiO_2 surface and their improved photocatalytic performance. *Appl. Surf. Sci.* **370**, 312–319 (2016).

Acknowledgements

Author contributions

R.A.E-G.: methodology, investigation, visualization, and writing—original draft. H.M.E-B.: conceptualization, methodology, investigation, resources, writing—review and editing, supervision, project administration, and funding acquisition. M.F.: conceptualization, methodology, investigation, resources, writing—review and editing, supervision, D.M.F.: review and editing, supervision.

Funding

Competing interests

The authors declare no competing interests.

Additional information

Supplementary Information The online version contains supplementary material available at https://doi.org/10.1038/s41598-023-34743-2.

Correspondence and requests for materials should be addressed to R.A.E.-G. or H.M.E.-B.

Reprints and permissions information is available at www.nature.com/reprints.

Publisher's note Springer Nature remains neutral with regard to jurisdictional claims in published maps and institutional affiliations.